Evolution of the bounded magnetized jet and comparison with Helimak experiments

R. B. Dahlburg,[1] W. Horton,[2] W. L. Rowan,[2] C. Correa,[2] and J. C. Perez[3]
[1]*Laboratory for Computational Physics and Fluid Dynamics, Naval Research Laboratory, Washington 20375-5344, USA*
[2]*Institute for Fusion Studies and Fusion Research Center, University of Texas at Austin, Austin, Texas 78712, USA*
[3]*Department of Physics, University of Wisconsin-Madison, Madison, Wisconsin 53706, USA*

(Received 23 January 2009; accepted 10 June 2009; published online 15 July 2009)

Magnetized jets are important features of many systems of physical interest. To date, most interest has focused on solar and space physics and astrophysical applications, and hence the unbounded magnetized jet, and its cousin, the unbounded magnetized wake, have received the most attention. This work presents calculations of a bounded, magnetized jet for a laboratory experiments in the Helimak device [K. W. Gentle and H. He, Plasma Sci. Technol. **10**, 284 (2008)]. The Helimak device has a toroidal magnetic field with a controlled velocity flow that represents jets in bounded systems. Experimental and theoretical features include three spatial dimensions, the inclusion of resistivity and viscosity, and the presence of no-slip walls. The results of the linearized model are computed with a Chebyshev-τ algorithm. The bounding walls stabilize the ideal varicose mode found in unbounded magnetized jets. The ideal sinuous mode persists in the bounded system. A comparison theorem is proved showing that two-dimensional modes are more unstable than the corresponding three-dimensional modes for any given set of system parameters. This result is a generalization of the hydrodynamic Squires theorem. An energy-stress theorem indicates that the Maxwell stress is crucial for the growth of the instability. The results of the analysis are consistent with the observed plasma fluctuations with in the limits of using a simple model for the more complex measured jet velocity flow profile. The working gas is singly ionized argon and the jet velocity profile is accurately measured with Doppler shift spectroscopy. [DOI: 10.1063/1.3166598]

I. INTRODUCTION

Many important physical systems can be modeled as magnetofluids with combined flow and magnetic shears. By combined flow and magnetic shears we denote a situation in which a sheared flow field and a sheared magnetic field are both present in close proximity.[1] This type of system is perhaps best illustrated by providing examples of the two canonical cases that have emerged: the magnetized jet[2] and the plane current-vortex sheet.[3] Both of these systems have sheared magnetic field structures. In the case of the magnetized jet, there is a fluid jet superimposed on the magnetic field structure. The magnetized jet has been used to model a variety of physical systems, including solar surges,[4,5] and the fast flows in Earth's magnetotail.[6] The magnetized jet can be turned into a magnetized wake by application of a Galilean transform. This closely related configuration has been used to model the formation and acceleration of the slow solar wind,[7] the heliospheric current sheet,[8] and nonthermal galactic jets.[9] This system with sheared magnetic fields and fast flows is frequently used to model solar surges[4] and tokamak plasmas with equilibrium flows.[10]

There are in addition many interesting laboratory plasma experiments with combined flows and magnetic shear, such as the Helimak[11] and the large plasma device[12] (LAPD) experiments. In general, these plasmas share the characteristic that they are bounded, as opposed to space and astrophysical plasmas in which boundaries are often so far away from the region of interest that they are ignored. Hence it is of interest to determine how the presence of walls alter the conclusions of previous research on magnetofluids with combined flow and magnetic shears. Are walls a stabilizing influence, or do walls serve as regions for destabilization and turbulence production? For example, many of the unstable modes found in earlier studies have been ideal, dissipationless instabilities. These modes are generally of large spatial extent in the cross-stream direction. Walls could disrupt the structure of these modes and alter their stability properties. Conversely, it has been found that walls can provide a source region for instabilities since large stresses can develop in response to the velocity or magnetic field striving to meet the imposed boundary condition. For example, in magnetized plane Poiseuille flow, large Reynolds and Maxwell stresses develop at the channel walls for the case of a dc magnetic field.[13] Kent[14] showed that sheared magnetic fields also strongly influenced the stability of magnetohydrodynamic (MHD) plane Poiseuille flow.

Early studies of magnetized channel flows are encouraging in that they indicate that there can be a significant interaction between sheared flows and magnetic fields in magnetofluids bounded in channels.[14,15] Interest in MHD plane Poiseuille flow[16,17] has waned somewhat so we study a representative system of contemporary interest. The Helimak experiment at the University of Texas at Austin is an excel-

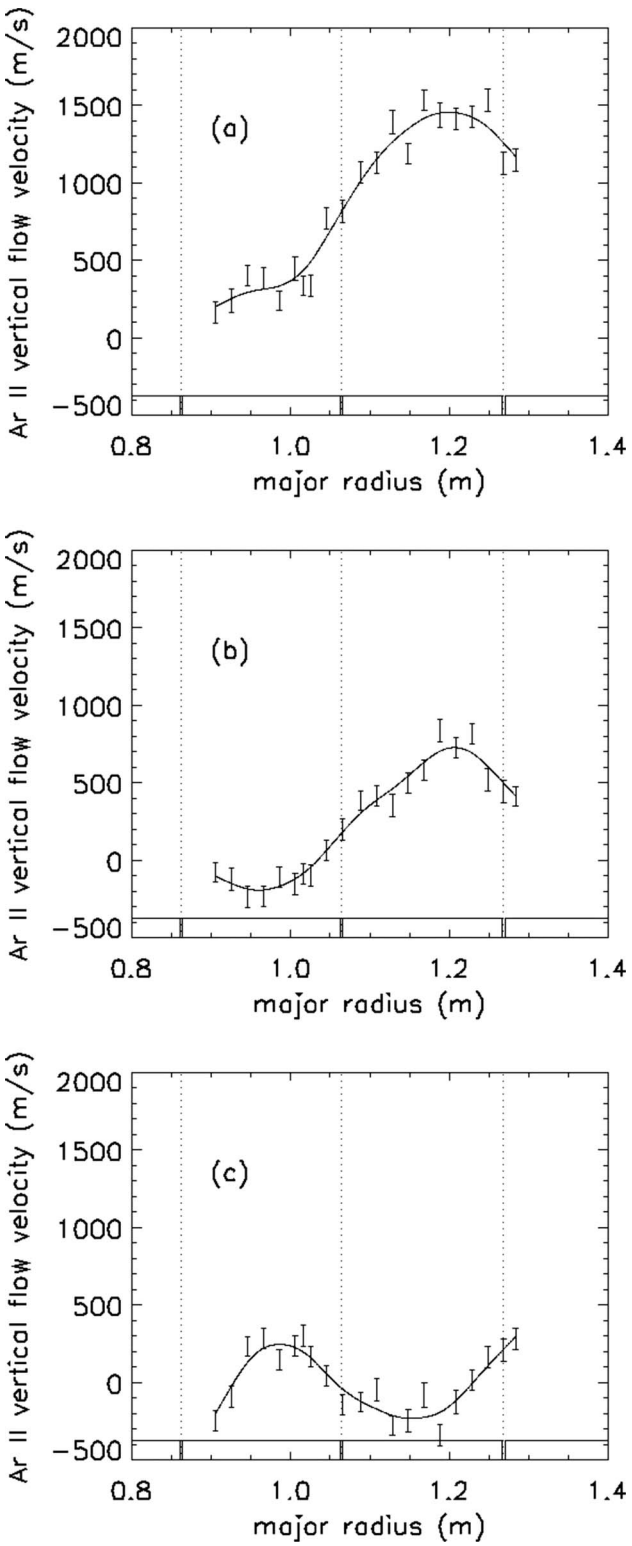

FIG. 1. Vertical flow profiles of a Helimak plasma at bias voltage values (a) $V_{\text{bias}}=0$, (b) $V_{\text{bias}}=-10$ V, and (c) $V_{\text{bias}}=-15$ V. The error bars correspond to the statistical uncertainty in spectroscopic Doppler shift measurements of spectral atomic emission lines from a working gas of singly ionized argon.

lent candidate. The Helimak is a toroidal magnetic confinement device designed to realize in the laboratory the sheared magnetic field slab geometry used by theorists in the analysis of localized modes in tokamaks.[11] When small resistive boundary layers are important it is not necessary for theory to keep the global radial profiles to study the plasma instabilities and turbulence. By virtue of the helical magnetic field structures modes with long parallel wavelengths $\lambda > 50-100$ m are allowed in the experiment. The Alfvén wave dynamics is thus part of the natural modes of the system and the fluctuations of the magnetic field are an important aspect of the system's dynamics as opposed to experiments with short lengths parallel to the magnetic field lines.

We show in this work that the sheared flows and magnetic fields of the Helimak can be classified as a bounded magnetized plasma jet. Hence we can use this system to see how the results of an earlier study of the unbounded magnetized jet are altered by the presence of walls.[3] In this work we focus on the linearized theory and calculation of MHD instabilities associated with a complex, sheared, bounded magnetofluid with flow and magnetic fields characteristic of the Helimak. We include the effects of resistivity and viscosity, as well as no-slip walls.[18] Linear theory will provide us with a guide to the parameter space of the Helimak. In particular, the stress analysis described in this paper gives us a better understanding of the energetics of Helimak flow and magnetic fields. In Fig. 1 we show three examples of the vertical flow $v_z=w(x)$ configurations created in the Helimak plasma with the data points and error bars from spectroscopic Doppler shift measurements of lines from the working gas of singly ionized argon. The flow profiles are controlled by the bias voltage V_{bias} given in the figure which changes the cross-field electric field E_r. The plasma responds in a complex manner to give the measured velocity profiles shown in frames a, b, and c for three values of the bias voltage. The profiles have velocity shear, and the associated vorticity dV_z/dr of order $(5\times10^3)-(1\times10^4\ \text{s}^{-1})$ changes sign at the inflection points in the profile. By virtue of the long lengths L of the magnetic field lines given by $L=B_\phi H/B_z>50$ m the Alfvén wave frequency is low $(k_\parallel v_A/2\pi\approx10$ kHz). Here $H=2$ m is the height of the plasma column and $B_\phi/B_z\approx0.1$ T/0.01 T is the ratio of the toroidal to vertical magnetic fields at midradius $r\approx1.1$ m from the vertical symmetry axis.

In Fig. 2, we show the fluctuation amplitudes of the electric potential and the electron density measured with Langmuir probes in the 10 eV argon plasma. The model used is incompressible, which is valid when the density fluctuations $\delta n/n$ are small compared to the dimensionless potential fluctuations. In the theoretical model, this occurs when the motions are resistive-viscous MHD-like with high v_E relative to the diamagnetic drift speeds. The probe data presented in Fig. 2 support this modeling since over most of the radial range shown, $e\Delta\phi/k_BT_e$ is twice as large as the fractional density fluctuations. The feature that $e\Delta\phi/k_BT_e \gg \delta n_e/n_e$ over much of the flow profile, or plasma jet, means that one may drop the drift wave terms to first order. The principal correction from adding the density fluctuations would be to introduce the electron diamagnetic frequency $\omega_{*e}=k_y(k_BT_e/eBL_n)$ to the fluctuations $(\omega\rightarrow\omega_{*e}+i\gamma)$.

Under the condition of weak compressibility, the parallel component of Ohm's law then simplifies to $E_\parallel=\eta j_\parallel$ in the modeling the experiment. The key fluctuations are the electric potential and perpendicular components of the magnetic

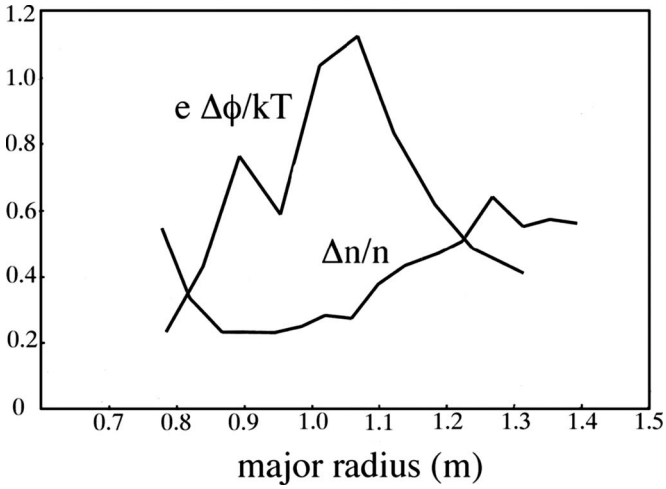

FIG. 2. Fluctuation amplitudes of the electric potential and the electron density measured with Langmuir probes in a 10 eV argon Helimak plasma.

field in these flow dominated plasmas. Owing to the large mass of the argon ions, these low temperature plasmas have $m_i\beta_e/m_e \simeq 1-2$, where β_e is the ratio of the electron thermal energy density to the magnetic energy density.

This article is organized as follows. In Sec. II we review some relevant results of research on the unbounded magnetized jet. In Sec. III we discuss the relation of the Helimak to the magnetized jet. In Sec. IV we examine the linear stability of the system, prove a MHD Squires theorem, and derive an energy-stress theorem for how the fluctuations received and give up energy in the bounded, magnetized jet. In Sec. V we discuss our results and consider some future directions for this research.

II. MAGNETIZED JET REVIEW: THE UNBOUNDED CASE

A first point to note is that a fluid jet can be transformed into a wake field by a Galilean transformation. This transformation can be achieved by moving to a frame of reference moving at the maximum jet speed in the original frame of reference. Hence studies of magnetized wakes are also relevant to the present paper. Unbounded magnetized jets and wakes have been studied in a variety of contexts. In general, researchers have investigated systems which are either magnetically dominated or flow dominated. It turns out that this is significant because the Alfvén number ($A=V_A/V_0$, where V_A is the characteristic Alfvén velocity and V_0 is the characteristic flow velocity) is very important in determining the evolution of the system (note that the inverse of the Alfvén number A, is the Alfvén Mach number, or $M_A=V_0/V_A$). For example, for the low A, or flow dominated plasmas, researchers have looked at the heliospheric current sheet, Earth's magnetotail, and at nonthermal galactic filaments. For the high A, or magnetically dominated case, researchers looked at solar surges and tokamaks. An interesting problem that requires investigation of both the high A and low A regimes is that of slow solar wind formation and acceleration. In this case the plasma originates in a magnetically dominated region below the solar Alfvén point, and then moves to a flow dominated region above the Alfvén point.

For flow dominated systems, with $0 \leq A \leq 1$, two unstable modes were found, an ideal varicose mode and a sinuous mode. A varicose mode is one in which the cross-stream flow is antisymmetric, and a sinuous mode is one in which the cross-stream flow is symmetric about the maximum or minimum of the flow profile. As A is increased these modes are stabilized. A generalization of the Howard semicircle theorem to the case of the magnetized jet showed that a strong enough magnetic field will suppress the ideal instabilities. As A increases above one, the system becomes magnetically dominated. In this case a resistive varicose mode was found. Note that in the fusion literature the sinuous mode would be denoted a kinklike mode and a resistive varicose mode would be called a tearinglike mode.

An analysis of the fluctuation energy-stress balance[2,3] shows that there are three stress components: the Reynolds stress, the Maxwell stress, and the cross-field stress. The values of the stresses and direction of energy flow is sensitive to the Alfvén number. We discuss these terms further in Sec. IV F for the case of the bounded magnetized jet. The Reynolds stress moderates the transfer of energy between the basic flow field and the perturbed flow field. The Maxwell stress moderates the transfer of energy between the basic flow field and the perturbed magnetic field. The cross stress, or dynamo term moderates the transfer of energy between the basic magnetic field and the perturbed flow and magnetic fields. The perturbed viscous dissipation determines the dissipative loss of perturbed kinetic energy. The perturbed Ohmic dissipation determines the dissipative loss of perturbed magnetic energy. The perturbed viscous and Ohmic dissipation was also affected by changes in A. In general, the resistive varicose mode is characterized by a large positive cross-stress contribution to the perturbed energy in the high A regime. For low A, the resistive varicose mode's cross-stress contribution is negative. The increase in a positive Maxwell stress contribution is not enough to compensate for increased Ohmic and viscous dissipation for low A, thus damping results. The ideal varicose mode has a large positive Maxwell stress contribution for all values of A. Again, dissipation increases for high A, resulting in damping. For the sinuous mode, the Reynolds stress is very large for low A. There is also a more modest contribution to the perturbed energy due to the Maxwell stress. As A increases, both of these processes are strongly damped, leading to stability.

As far as the nonlinear incompressible problem goes, most interest has focused on the magnetized wake due to its use as a model for several solar physics, space physics, and astrophysical situations. In two spatial dimensions, it has been found that moving plasmoids form and accelerate.[7] Of great interest has been the finding that the wake, or jet, spreads in the cross-stream direction and that its center line flow speed approaches that of the free-stream.[7] When the spanwise direction is included, secondary instabilities have been observed to occur, followed by a transition to turbulence.[5]

Compressibility represents a significant increase in complexity for this problem. The linearized equations are far

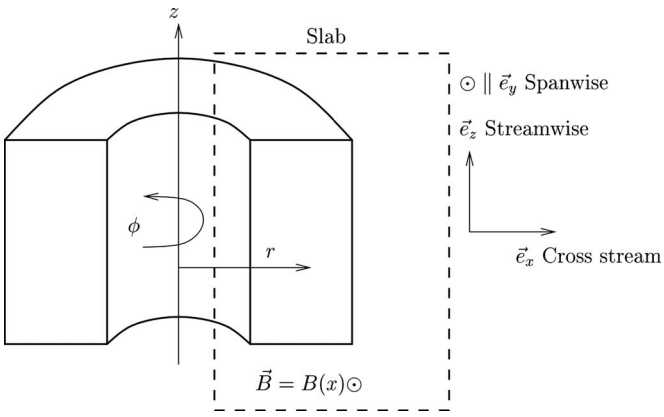

FIG. 3. A schematic drawing of the Helimak illustrating the coordinate system used in this paper.

more extensive. We find that three unstable modes occur.[19] Increasing the Mach number leads to decreased growth rates. In contrast with the current-vortex sheet, no second modes were found at high Mach numbers.[20] An interesting feature is that for certain situations, the three-dimensional (3D) ideal varicose modes grew at a faster rate than their two-dimensional (2D) counterparts.[19] In the nonlinear compressible problem, massive accelerated plasmoids have been observed.[21] These are similar to the incompressible plasmoids mentioned earlier, although the details of the acceleration are altered. Rappazzo *et al.* considered diamagnetic and expansion effects on this process.[22]

Based on our previous experience, in the present study of the bounded magnetized jet we focus first on the incompressible problem. This has proven to be a rather complex physical problem in our previous studies. We have found it profitable to study the linearized system to determine the principal modes of evolution, and then move on to the study of the two- and 3D nonlinear problems. Subsequently, the study of the even more complex compressible system is appropriate. The compressible linearized problem is much more complicated because the governing equations cannot be collapsed by invoking the solenoidal condition on the flow fields. We can then move on to the nonlinear compressible problem.[23–35]

III. HELIMAK AND ITS RELATION TO THE MAGNETIZED JET

A. Description of the Helimak experiment and its parameters

The slab geometry representation of the Helimak, shown schematically in Fig. 3, is similar to the MHD Poiseuille flow geometry[16,17] with concentric conducting walls at $r=a=0.6$ m and $r=b=1.6$ m and a height of $H=2$ m. The dominant toroidal field, B_ϕ, of order 0.1 T is produced by a set of 16 toroidal field coils around the vacuum chamber. Three other poloidal field coils are used to produce a weaker vertical field, B_z, which may be varied up to 10% of the toroidal field by changing the ratio of the current flowing through the toroidal coils to the current owing through the poloidal field coils. The magnetic field lines are thus helices spiraling from bottom to top and whose pitch varies with the radius as the toroidal field decreases as $1/r$, where r is measured from the vertical symmetry axis of the device. The field line length $L_\parallel$ may be varied from less than 20 m to more than 1 km by varying the strength of the vertical magnetic field B_z.

TABLE I. Helimak viscoresistive MHD parameters.

Toroidal magnetic field	$B_\phi=0.1$ T
Poloidal magnetic field	$B_z=0.01$ T
Half height	$H=1.0$ m
Half width	$L=0.5$ m
Aspect ratio	$H/L=2$
Magnetic field line length	$L_\parallel=20$ m
Argon density	$n_e=(2\times10^{10})-(2\times10^{11})$ cm^{-3}
Electron temperature	$T_e=10$ eV
Chamber volume	$V=13.8$ m^3
Space-time scale	$(L,T)=(0.5$ m$,0.6$ μs$)$
Magnetic diffusivity	$\eta/\mu_0=30$ m^2/s
Magnetic Reynolds number	$S_M=V_AL/(\eta/\mu)=10^4$
Ion kinematic viscosity	$\nu=0.3\rho_i^2\nu_i=0.3$ m^2/s
Viscous Reynolds number	$S_v=10^4$
Bohm diffusivity	$\chi_e=\frac{1}{16}\frac{T_e}{B}=6$ m^2/s

To create the jet, or localized flow $v_z=w(x)$, segmented end plates are biased to create various plasma flows across the magnetic field from the steady state radial electric field (E_r). Probe measurements of the radial electric field show localized E_r which means that there is a localized high speed vertical plasma stream in the vertical direction $\hat{e}_z$. Magnetic probes in the Helimak show a broad frequency spectrum of magnetic fluctuations.

The plasma studied has toroidal $B=0.1$ T, vertical or poloidal field from 0 to 05 T with electron cyclotron heating producing the ionized argon plasma with temperature of $T_e=10$ eV at the peak of the temperature profile. The plasma density ranges from 2×10^{16} to 2×10^{17} m^{-3}. For these parameter values and a density of 2×10^{17} m^{-3}, the computed Alfvén velocity is $(1-3)\times10^8$ cm/s, the resistivity is $\eta=10^{-5}$ Ω m and the kinetic viscosity is $\nu=10^4$ cm^2/s. More details on the plasma parameters are given in Table I. For this plasma we define the magnetic Reynolds number $S=V_Aa/(\eta/\mu_0)$ and the viscous Reynolds number $S_v=V_Aa/\nu$. Accordingly, we take $S=5000$ and $S_v=5000$ for the base line case and consider variations from these values in the analysis. The velocity of the argon ions Ar^{+1} is measured spectroscopically and is thus well known. Typical profiles are shown in Fig. 1. Singly ionized argon has emission lines in the blue part of the spectrum. The Doppler shift of these lines are measured to give accurate, well-resolved measurements of the ion velocity $v_z=w(x)$. The ion velocity is of the order 1 km/s and thus larger than the ion thermal velocity, comparable to the ion acoustic speed, and a significant fraction of the Alfvén velocity. Due to the large mass of the argon ions, $m_i\beta_e/m_e\approx1$, and electromagnetic fluctuations occur.

B. The slab model for the Helimak

In this paper we are exploring the behavior of a magnetofluid contained in a channel which corresponds to a slab model of the Helimak geometry. Hence it is appropriate to begin with a description of our slab, or channel, model and its relation to the Helimak. A schematic drawing of the Helimak and the slab coordinate systems is given in Fig. 3. In the laboratory frame of reference, we let x correspond to the radial direction, y' correspond to the toroidal direction, and z' correspond to the axial direction (since most of our research is performed in a rotated frame of reference, we use primes to denote the laboratory frame of reference). Periodic boundary conditions are imposed in the y' and z' directions and no-slip boundary conditions in the x direction, i.e.,

$$u'(x=\pm 1)=v'(x=\pm 1)=w'(x=\pm 1)=0, \tag{1}$$

where u' is the perturbed flow in the x direction, v' is the perturbed flow in the y' direction, and w' is the perturbed flow in the z' direction.

In the Helimak, most of the magnetic field is due to the currents flowing through the external coils, giving a base $1/r$ magnetic field,

$$B_\phi=\frac{B_0R_0}{r}=\frac{2aB_0}{b+a+(b-a)x}. \tag{2}$$

In our slab coordinate system, $x=0$ is located at the center of the channel. If we restrict the x coordinate to vary from $-1<x<1$, then the magnetic field can be written as

$$\mathbf{B}'_{0y'}(x)=\frac{1.2}{2.2+x}\hat{\mathbf{e}}_{y'},\quad \mathbf{B}'_{0z'}=0.1\hat{\mathbf{e}}_{z'}, \tag{3}$$

in which the magnetic field B'_{0y} is normalized to its value at Helimak's inner wall, i.e., $x=-1$, where $B_\phi(x=-1)=B_0$.

Probe measurements of the radial electric field show a localized radial E_r well which means that there is a localized high speed vertical plasma stream in the vertical direction $W'=E_r/B_\phi=W'_0(x)$. We model the $W(x)$ with a hyperbolic cosine function $\mathrm{sech}(r-r_0/w)\rightarrow\mathrm{sech}(3x)$. For the base line we take

$$\mathbf{V}'_0=0.0\hat{\mathbf{e}}_{y'},\quad \mathbf{W}'_0(x)=0.1\frac{\mathrm{sech}(3x)-\mathrm{sech}(3)}{\mathrm{sech}(0)-\mathrm{sech}(3)}\hat{\mathbf{e}}_{z'}, \tag{4}$$

where $\mathbf{V}'_0$ is the basic flow in the y' direction and $\mathbf{W}'_0$ is the basic flow in the z' direction. These fields are shown in Fig. 4.

C. Rotation to field-aligned coordinates

The model system has translational symmetry in the toroidal direction $\hat{\mathbf{e}}_{y'}$ and the vertical direction $\hat{\mathbf{e}}_{z'}$. Thus, the modes will be described by wavenumber vector $\mathbf{k}'=(0,\alpha',\beta')$. Both axisymmetric $\beta'=0$ and nonaxisymmetric toroidal mode numbers are investigated, where α' and β' correspond to the streamwise and spanwise wavenumbers, respectively, in the slab approximation in MHD. There is a continuum of Alfvén modes with $\omega=k_\parallel v_A$. The first modes to go unstable are often centered at $k_\parallel=0$, thus we actually look at a rotated field so that $\mathbf{k}\cdot\mathbf{B}(\mathbf{x}=\mathbf{0})=0$. The

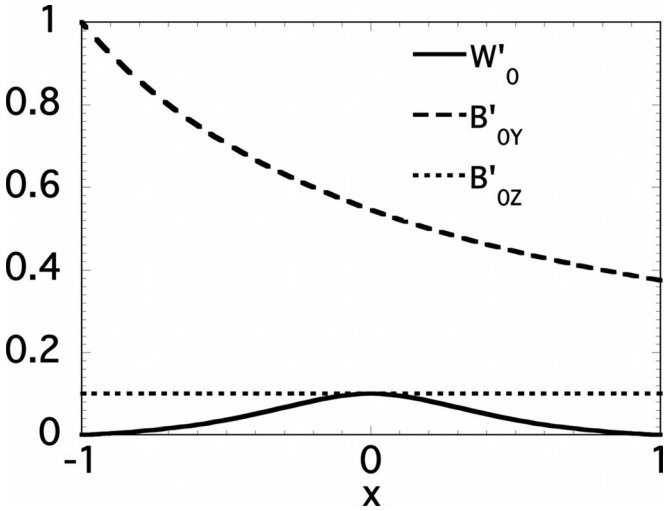

FIG. 4. Plot of the basic flow and magnetic field profiles for the calculations in this paper in the laboratory frame of reference. In the laboratory frame of reference x corresponds to the radial direction; y' corresponds to the toroidal direction; and z' corresponds to the axial direction (Since most of our research in performed in a rotated frame of reference, we use primes to denote the laboratory frame of reference). Note that the maximum flow speed is one-tenth of the maximum Alfvén speed.

rotation through the angle θ is in the $(\hat{\mathbf{e}}_{y'},\hat{\mathbf{e}}_{z'})$ plane such that $\mathbf{k}'\rightarrow\mathbf{k}$, $\mathbf{v}'\rightarrow\mathbf{v}$, and $\mathbf{B}'\rightarrow\mathbf{B}$. Hence in the rotated frame of reference we have for the magnetic field,

$$B_{0y}(x)\hat{\mathbf{e}}_y=B'_{0y'}\hat{\mathbf{e}}_{y'}\cos\theta+B'_{0z'}\hat{\mathbf{e}}_{z'}\sin\theta, \tag{5}$$

and

$$B_{0z}(x)\hat{\mathbf{e}}_z=-B'_{0y'}\hat{\mathbf{e}}_{y'}\sin\theta+B'_{0z'}\hat{\mathbf{e}}_{z'}\cos\theta, \tag{6}$$

and for the flow field we have

$$V_0(x)\hat{\mathbf{e}}_y=V'_0\hat{\mathbf{e}}_{y'}\cos\theta+W'_{0z'}\hat{\mathbf{e}}_{z'}\sin\theta=W'_{0z'}\hat{\mathbf{e}}_{z'}\sin\theta, \tag{7}$$

and

$$W_0(x)\hat{\mathbf{e}}_z=-V'_0\hat{\mathbf{e}}_{y'}\sin\theta+W'_0\hat{\mathbf{e}}_{z'}\cos\theta=W'_0\hat{\mathbf{e}}_{z'}\cos\theta. \tag{8}$$

For the rotation we want to have $\mathbf{k}\cdot\mathbf{B}(x=0)=0$. We can obtain this by rotating through an angle $\theta=\sin^{-1}[B'_z(x=0)/B'_y(x=0)]=\sin^{-1}[(-0.1\times 2.2)/1.2]$, which gives $\theta\approx-10.56°$. This rotation isolates the sheared magnetic field in the y-direction.

We adopt the following hydrodynamic terminology for the rotated coordinate system: The x-direction is referred to as the cross-stream direction, the y-direction is referred to as the streamwise direction, and the z-direction is referred to as the spanwise direction, Note that because of the small magnitude of the rotation employed ($\theta\approx-10.56°$), we can roughly identify the streamwise direction (y) with the toroidal direction, and the spanwise direction (z) with the axial direction.

The rotated fields are shown in Fig. 5. Note that the y-direction fields are a modified bounded form of the unbounded magnetized jet,[2] i.e., a fluid jet embedded in a sheared magnetic field. However, there are some interesting differences between the two cases that might lead to differences in evolution. As noted before, there are rigid bound-

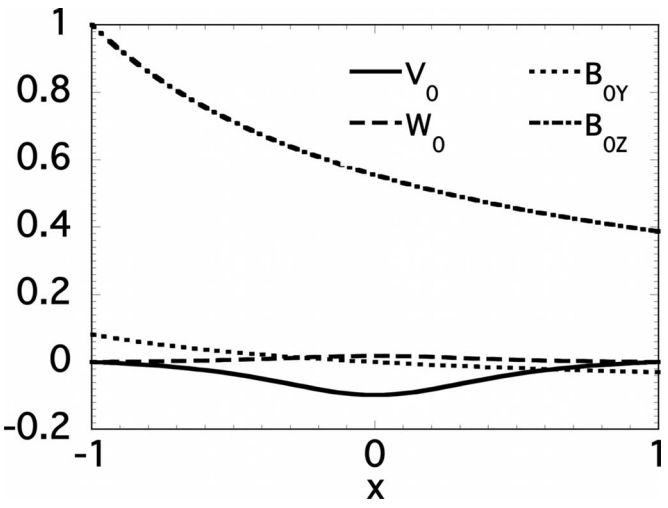

FIG. 5. Plot of the basic flow and magnetic field profiles for the calculations in this paper in the rotated frame of reference. The fields shown in Fig. 4 are rotated through an angle $\theta \approx -10.56°$ to move to the $\mathbf{k}\cdot\mathbf{B}=0|_{y=0}$ frame of reference. This is the frame of reference used for the calculations described in this paper.

aries in the channel problem. Boundaries can have both a stabilizing and a destabilizing influence. Another significant difference between the unbounded magnetized jet and the present fields is the lack of symmetry in the magnetic field. In particular, while the streamwise flow field is symmetric in x, the magnetic field is about three times larger at $x=-1$ than at $x=1$. This lack of symmetry influences the details of our numerical method, in that we must retain all of the Chebyshev polynomials to account for the asymmetry. We describe this numerical method more fully in Sec. IV. Finally, an examination of the y-direction fields alone in Fig. 5 might lead to the conclusion that this system is flow dominated since for these fields alone the characteristic flow speed exceeds the characteristic Alfvén speed. However, in terms of the total kinetic and magnetic energies, the system could also be described as magnetically dominated once the large z-direction magnetic field is taken into account. As we shall see, the linear dynamics appear to be best described as flow dominated. However, the guide field can have a large effect on the nonlinear dynamics.

IV. LINEAR CALCULATIONS

A. Derivation of linearized equations

First we consider the derivation of the linearized equations. We start with a dimensionless form of the nonlinear MHD equations,

$$\frac{\partial \mathbf{v}}{\partial t} = \mathbf{v} \times \zeta - \nabla \Pi + \mathbf{j} \times \mathbf{B} + \frac{1}{S_v}\nabla^2 \mathbf{v}, \tag{9}$$

and

$$\frac{\partial \mathbf{B}}{\partial t} = \nabla \times (\mathbf{v} \times \mathbf{B}) + \frac{1}{S}\nabla^2 \mathbf{B}, \tag{10}$$

together with the constraints: $\nabla\cdot\mathbf{v}=0$ and $\nabla\cdot\mathbf{B}=0$. In the above equations $\mathbf{v}(\mathbf{x},t)$ is the flow velocity, $\zeta(\mathbf{x},t)=\nabla\times\mathbf{v}$ is the vorticity, $\mathbf{B}(\mathbf{x},t)$ is the magnetic field, $\mathbf{j}(\mathbf{x},t)=\nabla\times\mathbf{B}$ is the electric current density, $\Pi(\mathbf{x},t)$ is the mechanical pressure+kinetic energy density per unit mass, and S is the Lundquist number, $S_v \equiv$ viscous Lundquist number (the resistivity and viscosity are assumed to be constant and uniform).[36,37] The velocities are measured in units of the Alfvén speed (V_A), and time is measured in units of the Alfvén transit time, l/V_A, where the characteristic distance l is defined as the channel half width. In this work we intentionally neglect the buoyancy instabilities associated with the pressure fluctuations in the curved magnetic fields to focus on the shear flow as a source of plasma turbulence in the resistive-viscous finite geometry system. Moreover, owing to Helimak's low ion temperature, the Hall effect from the separation of the ion drift velocity from the $\mathbf{E}\times\mathbf{B}$ drift velocity is negligible, hence $(\mathbf{v}-\mathbf{j}/en_e)\times\mathbf{B}=\mathbf{v}\times\mathbf{B}-(k_BT_e/e)\nabla \ln n_e$. Upon taking the curl of Ohm's law in the form $\mathbf{E}=\eta\mathbf{j}-(k_BT_e/e)\nabla \ln n_e$ for isothermal electrons, the electron pressure gradient drops out of Eq. (10) for $\partial B/\partial t$.

After linearizing Eqs. (9) and (10), and the solenoidality conditions of the state given in Eqs. (5)–(8), we decompose the first-order terms in the following manner:

$$a_1(x,y,z,t) = a(x)e^{i\alpha y + i\beta z - i\omega t}, \tag{11}$$

where α is the streamwise wavenumber, β is the spanwise wavenumber, and ω is the complex growth rate.

After eliminating the pressure, the equations which determine the linear modes are found. To write the equations compactly we define the operators $D\equiv d/dx$ and $\hat{\xi}=D^2-(\alpha^2+\beta^2)$, then the cross-stream (or radial) velocity (u) and magnetic induction (b_x) equations reduce to

$$\hat{\xi}^2 u - iS_vF\hat{\xi}u + iS_v(D^2F)u = -i\omega S_v\hat{\xi}u + iS_v[(D^2G)b_x - G\hat{\xi}b_x], \tag{12}$$

and

$$(\hat{\xi} - iSF + i\omega S)b_x = -iSGu, \tag{13}$$

with the boundary conditions: $u(x=\pm 1)=Du(x=\pm 1)=b_x(x=\pm 1)=0$. Here u and b_x are the x (radial) components of the perturbed velocity and magnetic field, respectively, $F=\alpha V_0+\beta W_0$ and $G=\alpha B_{0y}+\beta B_{0z}$ are the primary equilibrium velocity and magnetic fields. The remaining field components then are determined by using the solenoidality relations for the velocity and magnetic field.

Alfvén wave resonances occur from Eqs. (12) and (13) with $\omega^2=G^2(x)$ in the local limit with flow $F=0$ and no dissipation $1/S=1/S_v\to 0$. To get the 3D eigenfunction, we also solve perturbed vorticity $(\zeta=\beta v-\alpha w)$ and electric current $(\chi=\beta b_y-\alpha b_z)$ equations,

$$(\hat{\xi} - i\alpha S_vF)\zeta + i\alpha S_vG\chi = -i\omega S_v\zeta - \beta S_v[(DQ)v - (DP)b_y], \tag{14}$$

and

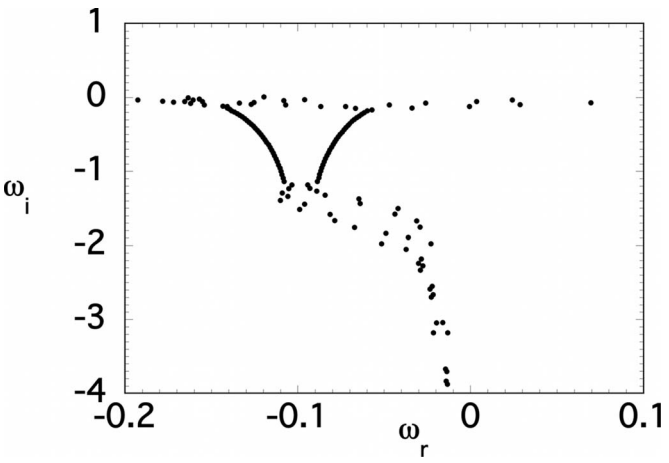

FIG. 6. The complete eigenmode spectrum for a typical axisymmetric vertical mode ($\alpha=2.3$, $\beta=0.0$, $S=S_v=5000$) for the reference flow profile given in Eqs. (5)–(8). Equations (12) and (13) are solved to obtain this solution.

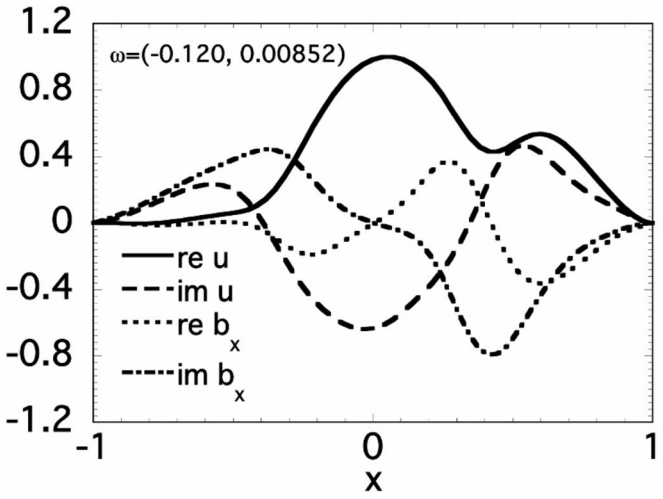

FIG. 7. The unstable eigenfunction for the bounded magnetized jet ($\alpha=2.3$, $\beta=0.0$, $S=S_v=5000$). This mode resembles the ideal sinuous mode found in the unbounded magnetized jet. For Helimak parameters the Alfvén time is 0.6 ms so the eigenmode has an angular frequency of 2×10^5 rad/s and a growth rate of 1.4×10^4 s^{-1}. It propagates perpendicular to the helical magnetic field at $x=0$ with $k_y=\alpha/r=4.6$ m^{-1}. This is well into the resistive MHD regime with $k_y\rho_s=0.014$.

$$(\hat{\xi}-i\alpha SF)\chi+i\alpha SG\zeta=-i\omega S\chi-\beta S[(DQ)b_y-(DP)v], \tag{15}$$

with the boundary conditions $\zeta(x=\pm1)=\chi(x=\pm1)=0$. Here v and w denote the streamwise and spanwise perturbed velocities, b_y and b_z denote the streamwise and spanwise components of the perturbed magnetic field, $P=\beta B_{0y}-\alpha B_{0z}$, and $Q=\beta V_0-\alpha W_0$.

B. Numerical method

We solve the linear equations with a Chebyshev-τ method.[38–40] The basic and perturbed fields are first expanded in truncated Chebyshev series, e.g., for the basic fields,

$$F(x)=\sum_{n=0}^{N}\tilde{F}_nT_n(x) \quad \text{and} \quad G(x)=\sum_{n=0}^{N}\tilde{G}_nT_n(x), \tag{16}$$

and for the perturbed fields,

$$u(x)=\sum_{n=0}^{N}\tilde{v}_nT_n(x) \quad \text{and} \quad b_x(x)=\sum_{n=0}^{N}\tilde{b}_nT_n(x). \tag{17}$$

$T_n(x)$ is the nth Chebyshev polynomial of the first kind and, for example, $\tilde{u}_n$ is the expansion coefficient of the perturbed velocity field.

The equations satisfied by the unknown expansion coefficients are obtained by substituting the $N\to\infty$ expansions of Eqs. (16) and (17) into Eqs. (12) and (13). Each equation produces a countably infinite number of equations in the expansion coefficients for $n=0,1,2,\ldots$ when the orthogonality and recursion relations are used.[38] We then set all coefficients beyond $n=N$ to zero and use the $n=0$ to $N-4$ equations from Eq. (12) and the $n=0$ to $N-2$ equations from Eq. (13) and the boundary conditions $\Sigma_{n=0}^{N}\tilde{v}_n=0$, $\Sigma_{n=0}^{N}(-1)^n\tilde{v}_n=0$, $\Sigma_{n=0}^{N}n^2\tilde{v}_n=0$, $\Sigma_{n=0}^{N}(-1)^nn^2\tilde{v}_n=0$, $\Sigma_{n=0}^{N}\tilde{b}_n=0$, and $\Sigma_{n=0}^{N}(-1)^n\tilde{b}_n=0$. This method of truncation is called the τ-approximation.[41] It differs from the Galerkin method in the test functions, e.g., Chebyshev polynomials, are not required to satisfy the boundary conditions. These are enforced by the inclusion of the boundary condition equations.

The spectral discretization process yields a generalized eigenvalue problem that can be written as $Ax=\omega Bx$, where the vector $x=(\tilde{v}_0,\tilde{v}_1,\ldots,\tilde{v}_N,\tilde{b}_0,\tilde{b}_1,\ldots,\tilde{b}_N)$ and A and B are nonsymmetric $(2N+2)$ by $(2N+2)$ square matrices.

As is customary for this type of stability problem, either global or local methods are used to determine the eigenvalues. For the global method we first transform the problem into the standard eigenvalue problem ($Cx=\omega x$), and then use the QR algorithm.[42] This produces a full spectrum of eigenvalues. When a good guess is available, local solutions are found using inverse Rayleigh power iteration. This converges to the eigenvalue (and its associated eigenfunction) closest to the initial guess for the eigenvalue. Generally we use the global method to identify the eigenvalue with the largest imaginary part (this is the most unstable mode or the least stable mode), and then use the local method to refine the eigenvalue and to compute the form of the eigenfunction. The local method is also used for examining how the solution changes as a parameter, for example, the Lundquist number, is varied.

C. Linear results: Spectrum, unstable eigenfunction, and dispersion relations

We now examine solutions of the linearized equations [Eqs. (12) and (13)]. For the base line Helimak case we use the following parameters: the streamwise wavenumber $\alpha=2.3$, the spanwise wavenumber $\beta=0.0$, the resistive Lundquist number $S=5000$, and the viscous Lundquist number $S_v=5000$. [As mentioned before, we can roughly identify the streamwise direction (y) with the toroidal direction, and the spanwise direction (z) with the axial direction in the Helimak. Our coordinate system is rotated $\approx-10.56°$ about the x direction shown in Fig. 3 to isolate the sheared mag-

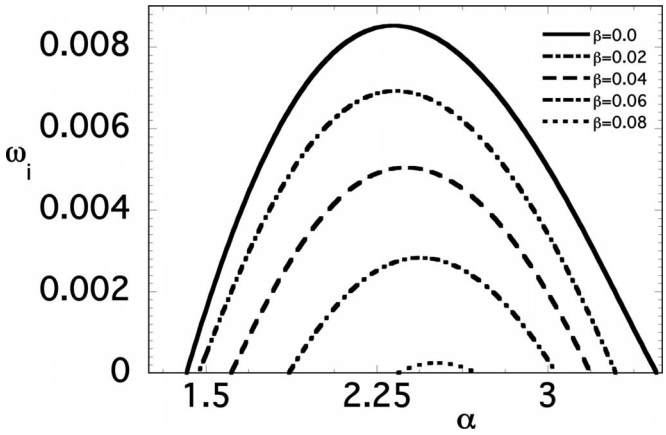

FIG. 8. Dispersion relations for the 2D case, parametrized by the spanwise wavenumber (β=0). For these calculations S_v=S=5000.

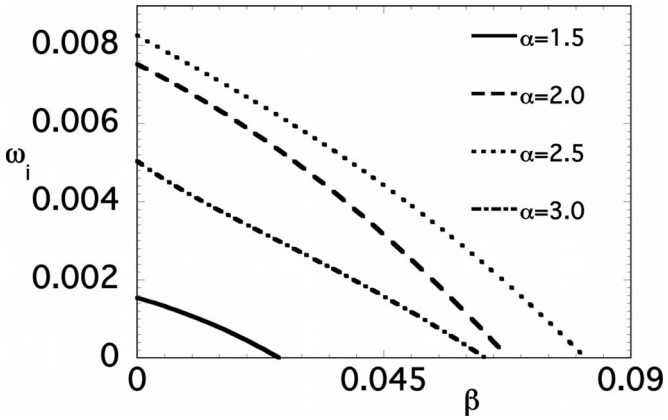

FIG. 9. Variation of growth rate with respect to spanwise wavenumber, parametrized by the streamwise wavenumber (α). For these calculations S_v=S=5000.

netic field component.] We will show later that this choice of α and β produces the largest growth rate for these values of S and S_v. The discrete eigenvalue spectrum is shown in Fig. 6 for this same set parameters. It can be seen that due to the presence of the basic streamwise flow, there are a large number of damped, traveling modes for these particular parameters. There is also one unstable traveling mode. The eigenfunction corresponding to this unstable mode is shown in Fig. 7. The form of the perturbed fields show that this is a global instability with comparable magnetic and flow velocity amplitudes. As mentioned before, the streamwise components of the rotated basic fields resembles the magnetized jet.[2] Three types of unstable mode have been identified for the magnetized jet: an ideal sinuous mode, an ideal varicose mode, and a resistive varicose mode. The sinuous mode magnetic field is kinklike in appearance, while for the varicose modes the magnetic field is sausagelike (ideal) or tearinglike (resistive). We find for the Helimak fields that the unstable mode is a somewhat distorted version of the sinuous mode reported for the magnetized jet.[2] In contrast with the magnetized jet sinuous mode, the Helimak mode is suppressed near the x=−1 wall, where the streamwise magnetic field is enhanced. There are no unstable ideal or resistive varicose unstable modes, as are seen in the magnetized jet, found for the Helimak fields. Note that the resistive varicose mode is a tearinglike mode which is expected to be stable in the Helimak. We now consider the dispersion relation. The variation of the growth rate ω_i with respect to α, parametrized by the spanwise wavenumber β, is shown in Fig. 8. We set S_v=S=5000 for these calculations. A nested family of curves is produced as the β is increased. All of the curves have the same form. This dispersion relation shows evidence of both low- and high-α cutoffs, as is typical for dissipative fluids confined to channels,[43] i.e., the lower cutoff is due to the finite channel width and the upper cutoff is due to the finite dissipation. It can be seen that the variation of β has several effects on the α dispersion relation. First, an increase in β generally leads to a decrease in the growth rate. We will return to this point later. Second, increasing β moves the maximum growth rate value to a larger value of α.

These variations of the growth rate (ω_i) with respect to the spanwise wavenumber β, parametrized by α, is shown in Fig. 9. We set S_v=S=5000 for these calculations. For all cases computed there is a cutoff value β_c above which the mode is stabilized. Note also that there is a decrease in the magnitude of the growth rate as β is increased. This implies that a Squires theorem[44–47] might be proved for the Helimak-like configuration, which we now proceed to do.

D. A magnetohydrodynamic Squires theorem

We prove that for the same wavenumber α, β and the same dissipation parameters S and S_v, the 2D system is more unstable than the 3D system. In hydrodynamics this theorem is well known as the Squires theorem. Thus, we show how the Squires theorem is generalized to a dissipative magnetohydrodynamical system. Hence, for the same S and S_v, the growth rate of the 2D unstable mode will be greater than that of the 3D unstable eigenmode.

After linearizing Eqs. (9) and (10) about the basic magnetic and flow fields, and then applying the eikonal decomposition, we are left with the following six coupled differential equations:

$$\{D^2-(\alpha^2+\beta^2)-iS_v(\alpha V_0+\beta W_0)+i\alpha S_v c\}u = S_v Dp - iS_v(\alpha B_{0y}+\beta B_{0z})b_x, \tag{18}$$

$$\{D^2-(\alpha^2+\beta^2)-iS_v(\alpha V_0+\beta W_0)+i\alpha S_v c\}v = i\alpha S_v p + S_v(DV_0)v - iS_v(\alpha B_{0y}+\beta B_{0z})b_y - S_v(DB_{0z})b_x, \tag{19}$$

$$\{D^2-(\alpha^2+\beta^2)-iS_v(\alpha V_0+\beta W_0)+i\alpha S_v c\}w = i\beta S_v p + S_v(DW_0)u - iS_v(\alpha B_{0y}+\beta B_{0z})b_z, \tag{20}$$

$$\{D^2-(\alpha^2+\beta^2)-iS(\alpha V_0+\beta W_0)+i\alpha Sc\}b_x = -iS(\alpha B_{0y}+\beta B_{0z})u, \tag{21}$$

$$\{D^2-(\alpha^2+\beta^2)-iS(\alpha V_0+\beta W_0)+i\alpha Sc\}b_x = S(DB_{0y})u - S(DV_0)b_x - iS(\alpha B_{0y}+\beta B_{0z})v, \tag{22}$$

and

$$\{D^2-(\alpha^2+\beta^2)-iS(\alpha V_0+\beta W_0)+i\alpha Sc\}b_z = S(DB_{0z})u - S(DW_0)b_x - iS(\alpha B_{0y}+\beta B_{0z})w, \quad (23)$$

where $c=\omega/\alpha$. The 2D problem is found by setting $\beta=0$ and $w=b_z=0$, or

$$\{D^2-\alpha^2+i\alpha S_v c\}u = S_v Dp - i\alpha S_v B_{0y} b_x + i\alpha S_v V_0 u, \quad (24)$$

$$\{D^2-\alpha^2+i\alpha S_v c\}u = i\alpha S_v p + i\alpha S_v V_0 v + S_v(DV_o)u - S_v(DB_{0y})b_x - i\alpha B_{0y} b_y, \quad (25)$$

$$\{D^2-\alpha^2+i\alpha Sc\}b_x = i\alpha S V_0 b_x - i\alpha S B_{0y} u, \quad (26)$$

and

$$\{D^2-\alpha^2+i\alpha S_v c\}b_y = i\alpha S B_{0y} u - i\alpha S V_0 b_y + S(DB_{0y})v - S(DV_0)b_x. \quad (27)$$

Can a transformation be found which casts Eqs. (18)–(23) in the same form as Eqs. (24)–(27)? Multiply Eqs. (19) and (22) by α, and multiply Eqs. (20) and (23) by β. Then add the new Eq. (20) to the new Eq. (19), and the new Eq. (23) to the new Eq. (22). This gives the following result:

$$\{D^2-(\alpha^2+\beta^2)-iS_v(\alpha V_0+\beta W_0)+i\alpha S_v c\}(\alpha v+\beta w) = iS_v(\alpha^2+\beta^2)p + S_v D(\alpha V_0+\beta W_0)u + S_v D b_x + i(\alpha B_{0y}+\beta B_{0z})(\alpha v+\beta w), \quad (28)$$

$$\{D^2-(\alpha^2+\beta^2)-iS(\alpha V_0+\beta W_0)+i\alpha S_v c\}(\alpha b_y+\beta b_z) = S_v D(\alpha B_{0y}+\beta B_{0z})u - iS(\alpha B_{0y}+\beta B_{0z})(\alpha v+\beta w). \quad (29)$$

Then apply a MHD version of the Squire transformation, i.e., define $\tilde{\alpha}\tilde{v}=\alpha v+\beta w$, $\tilde{\alpha}\tilde{b}_y=\alpha b_y+\beta b_z$, $\tilde{u}=u$, $\tilde{b}_x=b_x$, $\tilde{\alpha}=(\alpha^2+\beta^2)^{1/2}$, $\tilde{p}/\tilde{\alpha}=p/\alpha$, $\tilde{c}=c$, $\tilde{\alpha}\tilde{S}_v=\alpha S_v$, and $\tilde{\alpha}\tilde{S}=\alpha S$. First apply this transformation to Eqs. (18), (21), (28), and (29), then after dividing out a factor of $\tilde{\alpha}$ we are left with

$$\{D^2-\tilde{\alpha}^2+i\tilde{\alpha}\tilde{S}_v\tilde{c}\}\tilde{u} = i\tilde{\alpha}\tilde{S}_v\tilde{p} - i\tilde{\alpha}\tilde{S}_v B_0\tilde{b}_x - \tilde{S}_v(DB_0)\tilde{b}_z, \quad (30)$$

$$\{D^2-\tilde{\alpha}^2+i\tilde{\alpha}\tilde{S}_v\tilde{c}\}\tilde{w} = \tilde{S}_v D\tilde{p} - i\tilde{\alpha}\tilde{S}_v B_0\tilde{b}_z, \quad (31)$$

$$\{D^2-\tilde{\alpha}^2+i\tilde{\alpha}\tilde{S}_v\tilde{c}\}b_x = \tilde{S}_v(DB_0)\tilde{w} - i\tilde{\alpha}\tilde{S}B_0\tilde{u}, \quad (32)$$

and

$$\{D^2-\tilde{\alpha}^2+i\tilde{\alpha}\tilde{S}_v\tilde{c}\}b_z = -i\tilde{\alpha}\tilde{S}B_0\tilde{w}. \quad (33)$$

These equations have the same form as Eqs. (24)–(27) and hence define an equivalent 2D problem. Since $\tilde{\alpha}>\alpha$ for the 3D problem, the growth rate for the 3D problem is equal to the growth rate for a 2D problem at lower S and S_v. Hence, for the same S and S_v, the growth rate of the 2D unstable mode will always exceed that of the 3D unstable eigenmode Q.E.D.

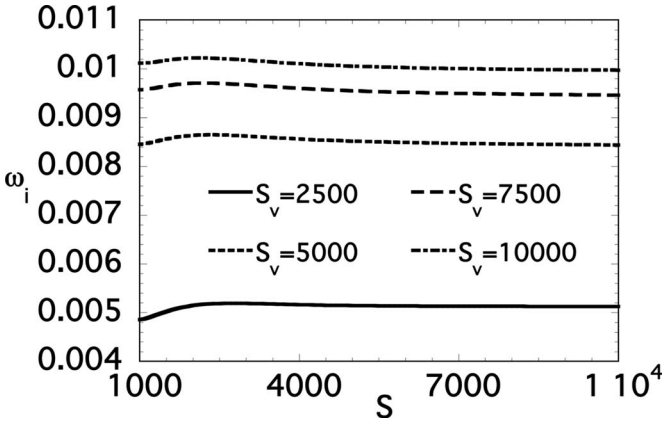

FIG. 10. Variation of growth rate with respect to Lundquist number (S), parametrized by the viscous Lundquist number (S_v). For these calculations $\alpha=2.3$ and $\beta=0.0$. Here $\omega_i=\mathrm{Im}(L\omega/v_A)$ corresponding to $\gamma\approx 10^4/\mathrm{s}$ for the parameters in Table I.

E. Effects of viscous and resistive dissipation

It is of interest to determine how viscous and Ohmic dissipation affect the evolution of the unstable mode, so next we will examine how the growth rate (ω_i) of the unstable mode varies with the resistive (S) and viscous (S_v) Lundquist numbers. Since we have denoted the unstable mode to be an "ideal sinuous mode" this might seem a little odd. However, by ideal we mean that neither viscosity or resistivity are needed for the instability to develop. Viscosity and resistivity can slow the rate of growth. As we will show, this effect will be insignificant at large values of S and S_v. Note that the expected values of S and S_v are limited to somewhat low values in the Helimak, e.g., $10^3\leq S\leq 10^4$ and $10^3\leq S_v\leq 10^4$, so that resistivity and viscosity could decrease growth rates from their values at $S\to\infty$ and $S_v\to\infty$. We will examine the variation of the growth rate within these bounds. The variation of the growth rate with respect to the Lundquist number (S), parametrized by the viscous Lundquist number (S_v), is shown in Fig. 10. The curves all exhibit the same general behavior. A small increase in the growth rate is seen as S increases from 1000, then there is a gradual decrease out to $S=10^4$. The $S_v=2000$ curve shows an increase out to approximately $S=2000$ and then slowly decreases. At least over this upper range of the Lundquist number we can say that the growth rate is almost independent of S, or, at most, very weakly dependent. However, the values of the growth rate are seen to change a lot between the curves with different values of S_v in Fig. 10, suggesting that ω_i is more sensitive to changes in S_v. Thus it is of interest to examine the variation of the growth rate with respect to viscous Lundquist number (S_v). This is shown in Fig. 11. Only curves for $S=2500$ and $S=10^4$ are shown because the various S curves do not show a lot of variation and tend to lie on top of each other. It is evident that over this range of values in S_v, there is a lot of change. It is of particular interest that stabilization is

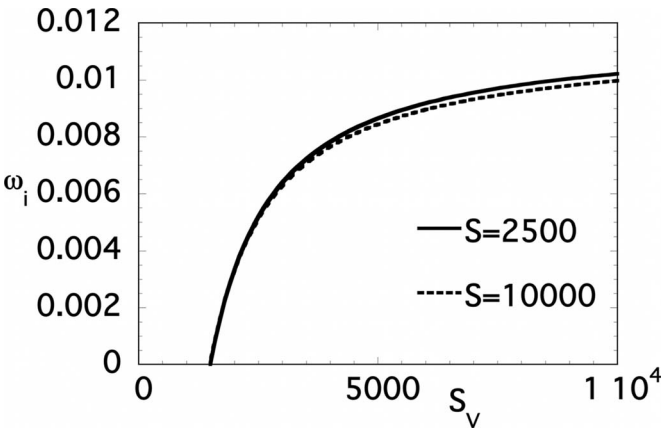

FIG. 11. Variation of growth rate with respect to viscous Lundquist number (S_v), parametrized by the Lundquist number (S). For these calculations $\alpha=2.3$ and $\beta=0.0$. Here $\omega_i=\mathrm{Im}(L\omega/v_A)$.

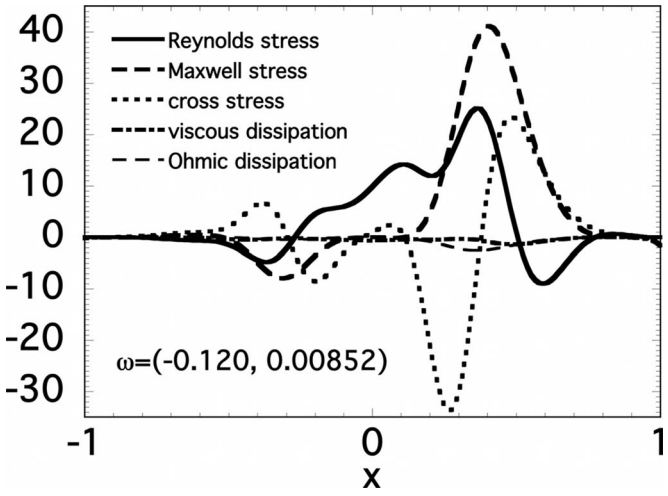

FIG. 12. Linear stresses for the model Helimak for the unstable mode shown in Fig. 7 ($\alpha=2.3$, $\beta=0.0$, $S=S_v=5000$).The Reynolds and Maxwell stresses dominate the other terms.

achieved for $S_v \approx 1500$, a region of parameter space accessible to the Helimak. As S_v increases, a monotonic increase in ω_i is seen. Above $S_v \approx 5000$ the rate of increase in ω_i slows considerably. The results suggest that increasing the value of the viscosity has a strong damping effect on the instability, whereas the growth of the instability is largely independent of the resistivity of the plasma.

Finally, we have adopted the terminology of our previous research in describing the unstable mode as the ideal sinuous mode. However, we have limited our discussion about the Lundquist numbers thus far to ranges which are relevant to the Helimak, i.e., $10^3 \le S \le 10^4$ and $10^3 \le S_v \le 10^4$. It is of interest to consider what happens for larger values of S and S_v. If the mode is ideal then its growth rate should show little variation for large S and S_v. From Figs. 10 and 11 it appears that there is relatively little change in the growth rate for larger values and that there could be a well defined growth rate in the inviscid limit $S_v \to \infty$, reinforcing our description of the sinuous mode as ideal. Another, less computationally intensive, way to approach this question is to see if the Rayleigh condition is satisfied. That is, does d^2V_0/dx^2 change sign within $-1 \le x \le 1$, i.e., within the slab? This is a necessary condition for ideal flow instability. It can be shown that d^2V_0/dx^2 does change sign in two places (we use our code and find the turning points at $x \approx \pm 0.29$). Hence the Rayleigh criterion is satisfied and the chosen flow profile is ideally unstable.

F. Perturbation energy analysis

We can gain some insight into what is happening in this ($\beta=0$) problem by a consideration of the energetics, a technique previously employed for the study of magnetized channel flows,[13,16] the current-vortex sheet,[3] and the magnetized jet.[2] The linear stresses and perturbed dissipation as functions of x are shown in Fig. 12 for the unstable eigenmode shown in Fig. 8. For the given system, the Reynolds stress is $-uv$; the Maxwell stress is $b_x b_y$; and the cross stress, or dynamo term, is $ub_y - vb_x$. These terms are described qualitatively in Sec. II and in further detail in Ref. 3. An examination of Fig. 12 indicates that the stresses all are significant while the perturbed dissipation remains relatively small. Bear in mind, however, that it is the net effect of the stress that is important to the growth of the perturbation. Changes in sign of the stress terms indicates that the energy transfer is not a one-way process. There are spatial regions of the flow channels where the basic fields pump energy into the fluctuating fields. The process is reversed elsewhere in the flow channels. As far as growth of the perturbation goes, it is the net energy transfer that counts. Note also that the stresses are all at their largest values in the interior of the flow channel (especially at the high field, or inner, wall side), so it appears that the walls exert only a minimal effect on the energy transfers.

The perturbation energy balance for this 2D problem is given by

$$\frac{1}{2}\frac{d}{dt}\int_{-1}^{1}\int_{0}^{2\pi/\alpha}(u^2+v^2+b_x^2+b_y^2)dydx$$
$$=-\int_{-1}^{1}\int_{0}^{2\pi/\alpha}uv\frac{dV_0}{dx}dydx$$
$$+\int_{-1}^{1}\int_{0}^{2\pi/\alpha}b_x b_y\frac{dV_0}{dx}dydx$$
$$+\int_{-1}^{1}\int_{0}^{2\pi/\alpha}(ub_y-vb_x)\frac{dB_{0y}}{dx}dydx$$
$$-\frac{1}{S_v}\int_{-1}^{1}\int_{0}^{2\pi/\alpha}\zeta^2 dydx-\frac{1}{S}\int_{-1}^{1}\int_{0}^{2\pi/\alpha}j^2 dydx. \quad (34)$$

Here ζ is the perturbed vorticity and j is the perturbed electric current. The first term on the right hand side of Eq. (34) represents contributions to the perturbed kinetic energy due to Reynolds stress. If this term is positive, it implies that the perturbation is gaining energy from V_0. If this term is negative, it implies that the perturbation is feeding energy into V_0. The second term determines contributions due to the Maxwell stress, which represents an energy exchange be-

tween the perturbed magnetic field and V_0. The third term contains the effect of the cross stress, which determines the exchanges of energy between the perturbation and B_{0y}. The fourth term represents energy losses due to viscous dissipation, and the fifth term determines the energy lost due to Joule heating. These last two terms are always negative. The growth rate of the perturbation depends on the sum of all these integral terms: Growth only results if the sum of all of these terms is positive. With two background fields, this allows for some complicated behavior. For example, the perturbation could lose energy to V_0, but still gain enough energy from B_{0y} to grow.

We can evaluate the terms in Eq. (34) by using the eigenfunctions obtained from solving the eigenvalue problem. After some algebra and separating the fields into the real and imaginary parts u_r, u_i, b_{xr}, and b_{xi} we are left with

$$\frac{\gamma}{\alpha}\int_{-1}^{1}\left(\left|\frac{du}{dx}\right|^2+\alpha^2|u|^2+\left|\frac{db_x}{dx}\right|^2+\alpha^2|b_x|^2\right)dx$$
$$=-\int_{-1}^{1}\left(-u_i\frac{du_r}{dx}+u_r\frac{du_i}{dx}\right)\frac{dV_0}{dx}dx+\int_{-1}^{1}\left(b_{xi}\frac{db_{xr}}{dx}-b_{xr}\frac{db_{xi}}{dx}\right)\frac{dV_0}{dx}dx+\int_{-1}^{1}\left(\frac{du_r}{dx}b_{xi}-\frac{du_i}{dx}b_{xr}-u_i\frac{db_{xr}}{dx}+u_r\frac{db_{xi}}{dx}\right)\frac{dB_{0y}}{dx}dx$$
$$-\frac{1}{\alpha S_v}\int_{-1}^{1}\left[\left(\frac{d^2u_r}{dx^2}-\alpha^2u_r\right)^2+\left(\frac{d^2u_i}{dx^2}-\alpha^2u_i\right)^2\right]dx-\frac{1}{\alpha S}\int_{-1}^{1}\left[\left(\frac{d^2b_{xr}}{dx^2}-\alpha^2b_{xr}^2\right.\right.\left.\left.+\left(\frac{d^2b_{xi}}{dx^2}-\alpha^2b_{xi}\right)^2\right]dx, \tag{35}$$

where γ is the energy-based growth rate.

Let us consider the terms in Eq. (35) for a moment, neglecting the dissipation. In the neutral fluid limit only the Reynolds stress term survives. This term governs the energy exchanges that drive the Kelvin–Helmholtz instability. In cases in which there is a basic magnetic field but no mean flow $V_0(x)$ the parts of the cross-stress term containing both b_{xr} and u_i survive. These are the terms that are important for Alfvén waves and resistive instabilities. The new features in the combined case considered in this paper are the Maxwell stress term and the parts of the cross-stress term containing b_{xi} and u_r. Thus, the phases of the fields are now important, which increases the complexity of the flow patterns.

We can rewrite Eq. (35) symbolically as

$$\gamma E=\alpha I_1+\alpha I_2+\alpha I_3-\frac{1}{S_v}I_4-\frac{1}{S}I_5. \tag{36}$$

We then can solve for the perturbation energy-based growth rate (γ),

$$\gamma=\alpha\frac{I_1}{E}+\alpha\frac{I_2}{E}+\alpha\frac{I_3}{E}-\frac{1}{S_v}\frac{I_4}{E}-\frac{1}{S}\frac{I_5}{E}=T_R+T_M+T_C+\Omega+J. \tag{37}$$

Here T_R, T_M, T_C, Ω, and J represent normalized versions of the perturbed energy contributions due to the Reynolds stress, Maxwell stress, cross stress, viscous dissipation, and Ohmic dissipation, respectively. The stress terms T_R, T_M, and T_C can be positive or negative depending on whether energy is being transferred from the basic field to the perturbed field, or vice versa. The dissipative terms Ω and J are always negative and thus subtract energy from the perturbation.

We now compare the energy-based γ to the growth rate (ω_i) computed by solution of the eigenvalue problem to determine the accuracy of this analysis. Typically the relative error is less than one percent. For example, for the case shown in Fig. 12, the growth rate, computed from the linearized equations [Eqs. (12) and (13)] using 189 Chebyshev polynomials, is 0.008 52. For comparison, direct computation from Eq. (37) gives the results T_R=0.006 540, T_M=0.013 98, T_c=0.000 072 70, Ω=−0.005 516, and J=−0.006 572. Adding these up, results in $\gamma\approx$0.008 50. Thus the growth rate based on the stress computation has as error of ≈0.1%. Finally, note that the stresses are largest in the interior of the flow channel, and that that they remain close to zero near the walls. This implies that the walls are relatively insignificant in the linear evolution of the unstable mode.

We can use the terms in Eq. (37) to figure out why the perturbed modes are damped out when, for example, the streamwise wavenumber (α) becomes too large or too small. These various terms, along with the growth rate, are shown for the sinuous case in Fig. 13 as a function of the streamwise wavenumber (α). First, it is apparent from this figure that the major contributor to the growth of the perturbation is the Maxwell stress term, i.e., the basic flow is pumping energy into the perturbed magnetic field. The Reynolds stress term is smaller in magnitude, and only positive over a limited range of α. For those regions where it is negative, the perturbed flow field is pumping energy into the basic field. The cross-stress term remains negligible over all α relative to the Maxwell stress. Figure 13 indicates that the stabilization and eventual damping of the mode at low α occur primarily because of a decrease in the Maxwell stress term. The stabilization and eventual damping at large α occurs because of an increase in the magnitude of the perturbed viscous and Ohmic dissipation. A decrease in the Reynolds stress term also contributes to the decrease in the growth rate.

Now let us apply the same analysis to the damping observed at low values of the viscous Lundquist number (S_v).

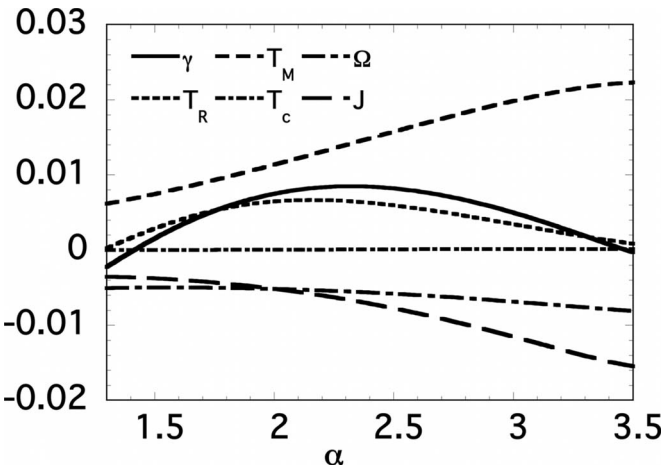

FIG. 13. Variation of perturbation energy balance terms with respect to streamwise wavenumber. Here the *y*-axis γ is the growth rate in units of v_A/L and, T_R, T_M, T_C, Ω, and J are the normalized values of the fluctuation energy contributions due to the Reynolds stress, Maxwell stress, cross stress, viscous dissipation, and Ohmic dissipation, respectively. For these calculations $\beta=0.0$ and $S=S_v=5000$.

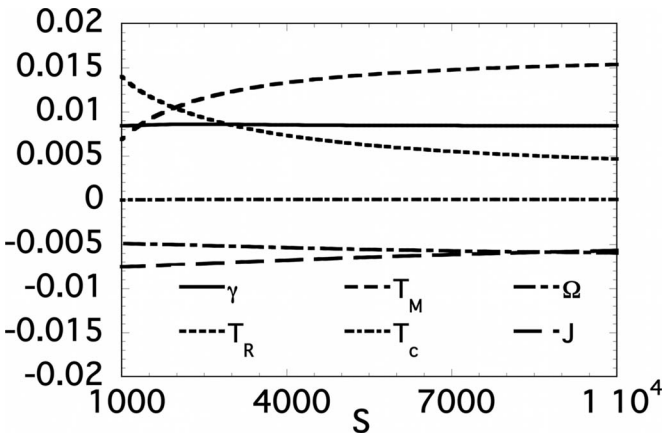

FIG. 15. Variation of perturbation energy balance terms with respect to Lundquist number (S). Here γ is the growth rate and T_R, T_M, T_C, Ω, and J represent normalized versions of the perturbed energy contributions due to the Reynolds stress, Maxwell stress, cross stress, viscous dissipation, and Ohmic dissipation, respectively. For these calculations $\alpha=2.3$, $\beta=0.0$, and $S_v=5000$.

These stress and dissipation terms, along with the growth rate, are shown for the sinuous case in Fig. 14 as a function of the viscous Lundquist number. Again, the major contributor to the growth rate is the Maxwell stress term. This term actually increases as S_v decreases, but this is basically canceled out by the Ohmic dissipation (J). All of the other terms contribute to the damping effect. The Reynolds stress term becomes negative below $S\approx 5000$, and there is a small increase in the magnitude of the viscous dissipation as well.

This energy analysis can also be used to determine why the growth rate increases as the Lundquist number is decreased down to about 2000, as seen in Fig. 10. The results of a perturbation energy analysis are shown in Fig. 15. For large S, the major contributor to the perturbed energy is T_M.

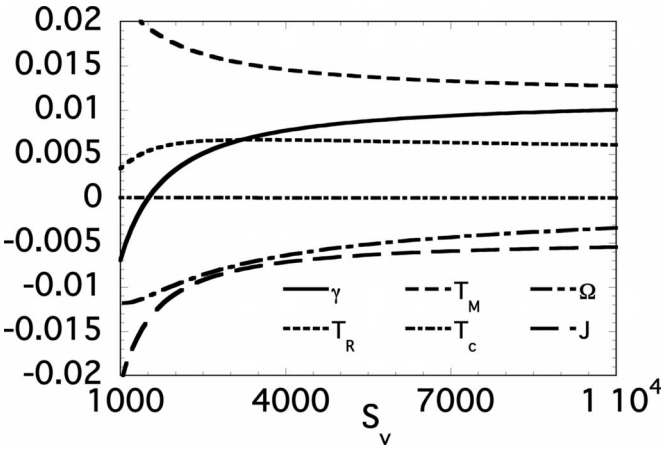

FIG. 14. Variation of perturbation energy balance terms with respect to viscous Lundquist number (S_v). Here γ is the growth rate and, T_R, T_M, T_C, Ω, and J represent normalized versions of the perturbed energy contributions due to the Reynolds stress, Maxwell stress, cross stress, viscous dissipation, and Ohmic dissipation, respectively. For these calculations $\alpha=2.3$, $\beta=0.0$, and $S=5000$.

As S is decreased, T_M also decreases, while T_R increases. Thus an increase in the Reynolds stress contribution leads to an increase in ω_i as S is decreased, at least for $S>2000$.

V. DISCUSSION

This work investigates the details of the low frequency electromagnetic modes in a bounded, multiple sheared, viscoresistive magnetofluid. Among our objectives was to determine if and how the presence of walls modifies the results and conclusions of our previous studies of unbounded magnetized jets.[3] The Helimak configuration was chosen because it produces a bounded magnetized jet with a long effective parallel length $L=HB_\phi/B_z$ of great contemporary interest.

We found that bounded magnetized jets do evolve differently than unbounded magnetized jets. For the Helimak fields and parameters, the system is flow dominated for the linear case. Based on the unbounded jet results, there are two unstable modes for this case, an ideal sinuous (kinklike) mode and an ideal varicose mode. For the bounded jet case reported in this work, we find only one unstable sinuous mode. This unstable mode strongly resembles the ideal sinuous mode found for the unbounded magnetized jet.[3] An unstable ideal varicose mode is not found. Both high and low streamwise wavenumber (α) cutoffs are found for the ideal sinuous mode. This mode is driven by the velocity shear and thus is relatively insensitive to variations in the resistive Lundquist number (S), but it can be stabilized for values of the viscous Lundquist number (S_v) that are accessible in the Helimak.

We performed a stress analysis to obtain some insight into the transfer of energy between the perturbed fields and the basic fields. A low streamwise wavenumber cutoff occurs due to a decrease in the Maxwell stress. A high streamwise wavenumber cutoff occurs, as expected, because of an increase in viscous and Ohmic dissipation. We found that the stabilization with the viscous Lundquist number occurs due to increases in the magnitude of both the viscous and Ohmic

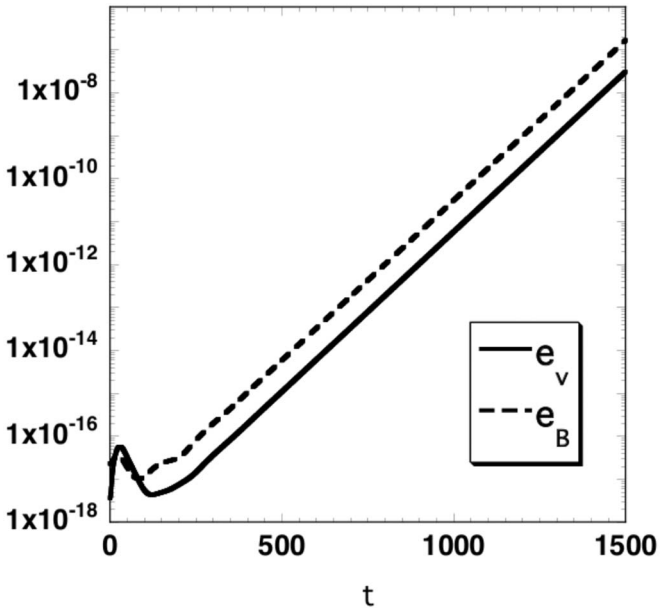

FIG. 16. Fluctuating kinetic energy (e_v) and fluctuating magnetic energy (e_B) for a simulation with the same parameters as those used in Fig. 7. The results shown here are computed using a 3D, nonlinear Chebyshev collocation-Fourier pseudospectral code that solves Eqs. (9) and (10) in a channel geometry. An exponential phase of growth is seen to occur in both e_v and e_B after about 200 characteristic times.

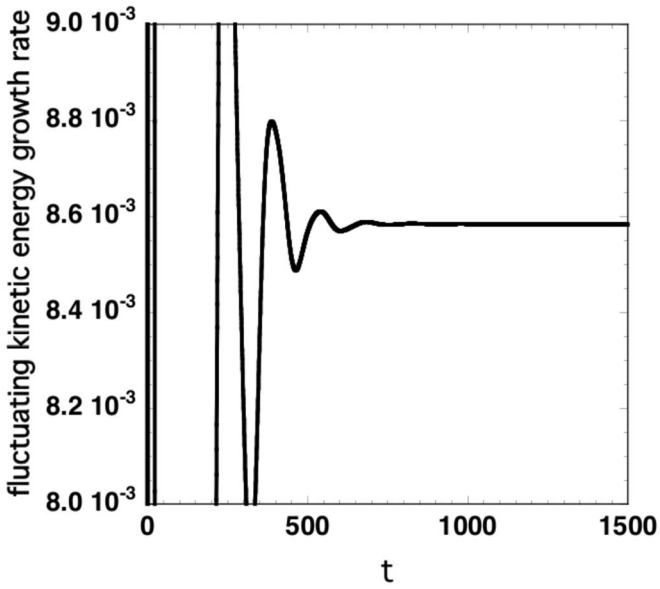

FIG. 17. Fluctuating kinetic energy growth rate as a function of time computed from the result shown in Fig. 16. This case uses the same parameters as are used in Fig. 7. Note that the growth rate computed from the linearized equations [Eqs. (12) and (13)] is 0.008 52.

dissipation, as well as a decrease in the Reynolds stress, as the viscous Lundquist number is decreased. We found numerically that at least linearly, the 2D modes are the most dangerous. A rigorous demonstration of this point is given by our proof of a generalized MHD Squires theorem. However, the 3D modes may be more important for the dynamo processes and for magnetic reconnection. The laboratory signature of these unstable sinuous modes is the presence of correlated magnetic (b_x) and flow (v_x) fluctuations that increase in amplitude with the strength of the flow shear (dV_0/dr) and its curvature (d^2V_0/dr^2).

We plan to follow up these linear calculations with some nonlinear simulations and analyses. The results presented in the present work are useful guides for the nonlinear simulations. We have developed a 3D Chebyshev collocation-Fourier pseudospectral code called MHDCHAN for these nonlinear simulations. We will describe this code in detail in a latter publication (a 2D electrostatic drift wave version is described in Ref. 48). To illustrate the utility of the present calculations we show here some results, using the nonlinear MHDCHAN code, of the time evolution of small perturbations in the basic bounded magnetized jet fields given by Eqs. (3) and (4). Figure 16 shows the fluctuating kinetic energy (e_v) and fluctuating magnetic energy (e_B) for a simulation with the same parameters as those used in Fig. 8. This simulation is run with four Fourier modes in each of the periodic directions (x and y) and 64 Chebyshev modes in the cross-stream direction (z). Hence the linear behavior should be resolved and the simulation should break down as the fluctuating fields attain finite amplitude. Figure 16 shows that after about 200 Alfvén times both e_v and e_B enter into a period of growth that appears to be exponential. The computed growth rate for e_v as a function of time is shown in Fig. 17. Recall that the growth rate computed for these parameters is based on the solution of the linearized equations [Eqs. (12) and (13)] was 0.008 52. The kinetic energy growth rate at late times shown in Fig. 17 is close to this, lending support to the linearized calculations. In Fig. 18 we show the results of computation of the stress terms given in Eq. (37). Note that the stress and dissipation terms settle down to values close to those given by the eigenvalue computation.

We plan to investigate the full 3D nonlinear evolution of the bounded magnetized jet more thoroughly in a subsequent

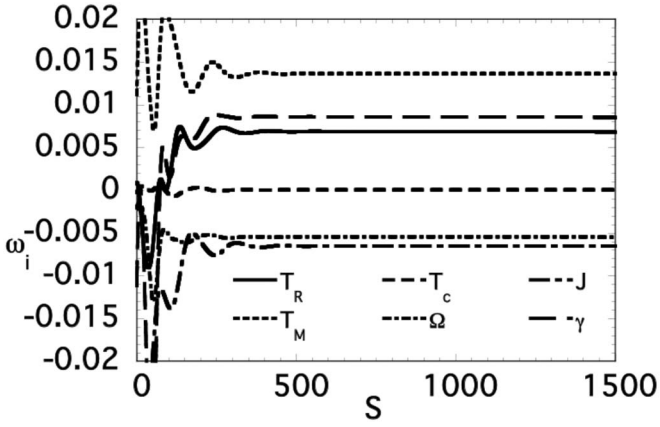

FIG. 18. Perturbation energy balance stress components as functions of time as given by Eq. (37). This case uses the same parameters as are used in Fig. 7. Here T_R is the Reynolds stress term, T_M is the Maxwell stress term, T_C is the cross-stress term, Ω is the viscous dissipation term, and J is the Ohmic dissipation term. The growth rate determined from addition of these components is γ. For comparison, direct computation from Eq. (37) gives the results: T_R=0.006 540, T_M=0.013 98, T_c=0.000 072 70, Ω=−0.005 516, and J=−0.006 572. Adding these up, we compute that $\gamma \approx 0.008\ 50$. Note as well that the growth rate computed from the linearized equations [Eqs. (12) and (13)] is 0.008 52.

publication. The results of linear stability analyses for channel flows are often widely divergent from experimental results.[43,49] In particular, the linear results for plane Poiseuille flow and plane Couette flow do not mesh well with the actual behavior of pressure driven and wall driven channel flows. Other cases of evolution, such as rotating Couette flow and flat plate boundary layers, are well described by linear analysis. In general, it is desirable to include nonlinearity and three dimensionality to account for experimental results. Three dimensionality and nonlinear interactions are crucial for turbulence and the transition to turbulence. In a subsequent paper we will consider the nonlinear evolution of the system described in the present paper. It is also important to advance to the compressible extension of this system to allow for the inclusion of the resistive interchange instabilities driven by magnetic curvature in the Helimak and solar corona configurations.

ACKNOWLEDGMENTS

The authors would like to thank T. A. Zang for helpful discussions and acknowledge useful discussion with Professor Ken Gentle on the physics of the Helimak device.

R.B.D. was supported by the Office of Naval Research. W.H., C.C., and J.P. were supported by the U.S. Department of Energy contract DE-FG02-04ER 54742 and NSF Grant ATM-0539099. W.R. was supported by DE-NSF. The numerical computations were performed on the LCP&FD SGI Origin 3400.

[1] K. W. Gentle and H. He, Plasma Sci. Technol. **10**, 284 (2008).
[2] R. B. Dahlburg, P. Boncinelli, and G. Einaudi, Phys. Plasmas **5**, 79 (1998).
[3] R. B. Dahlburg, P. Boncinelli, and G. Einaudi, Phys. Plasmas **4**, 1213 (1997).
[4] V. Carbone, G. Einaudi, and P. Veltri, Sol. Phys. **111**, 31 (1987).
[5] R. B. Dahlburg and J. T. Karpen, Astrophys. J. **434**, 766 (1994).
[6] T. Sato and R. J. Walker, J. Geophys. Res. **87**, 7453, DOI: 10.1029/JA087iA09p07453 (1982).
[7] G. Einaudi, P. Boncinelli, R. B. Dahlburg, and J. T. Karpen, J. Geophys. Res. **104**, 521, DOI: 10.1029/98JA02394 (1999).
[8] S. Wang, L. C. Lee, C. Q. Wei, and S.-I. Akosofu, Sol. Phys. **117**, 157 (1988).
[9] R. B. Dahlburg, G. Einaudi, T. N. LaRosa, and S. N. Shore, Astrophys. J. **568**, 220 (2002).
[10] R. B. Paris and W. N.-C. Sy, Phys. Fluids **26**, 2966 (1983).
[11] J. C. Perez, W. Horton, K. Gentle, W. L. Rowan, K. Lee, and R. B. Dahlburg, Phys. Plasmas **13**, 032101 (2006).
[12] W. Horton, J. C. Perez, T. Carter, and R. Bengston, Phys. Plasmas **12**, 022303 (2005).
[13] P. R. Nachtsheim and E. Reshotko, NASA Technical Note No. d-3144, 1965. Copies may be ordered from the NASA Technical Reports Server, National Aeronautics and Space Administration, Washington D.C. 20546.
[14] A. Kent, Phys. Fluids **9**, 1286 (1966).
[15] M. E. Stern, Phys. Fluids **6**, 636 (1963).
[16] J. T. Stuart, Proc. R. Soc. London, Ser. A **221**, 189 (1954).
[17] E. P. Velikhov, Sov. Phys. JETP **36**, 848 (1959).
[18] R. B. Dahlburg, Phys. Plasmas **5**, 133 (1998).
[19] R. B. Dahlburg, R. Keppens, and G. Einaudi, Phys. Plasmas **8**, 1697 (2001).
[20] R. B. Dahlburg and G. Einaudi, Phys. Plasmas **7**, 1356 (2000).
[21] G. Einaudi, S. Chibbaro, R. B. Dahlburg, and M. Velli, Astrophys. J. **547**, 1167 (2001).
[22] A. F. Rappazzo, M. Velli, G. Einaudi, and R. B. Dahlburg, Astrophys. J. **633**, 474 (2005).
[23] D. H. Michael, Proc. Cambridge Philos. Soc. **51**, 528 (1955).
[24] W. I. Axford, Q. J. Mech. Appl. Math. **13**, 314 (1960).
[25] D. H. Michael, Proc. Cambridge Philos. Soc. **57**, 628 (1961).
[26] G. Einaudi and F. Rubini, Phys. Fluids **29**, 2563 (1986).
[27] G. Einaudi and F. Rubini, Phys. Fluids B **1**, 2224 (1989).
[28] J. T. Karpen, S. K. Antiochos, R. B. Dahlburg, and D. S. Spicer, Astrophys. J. **403**, 769 (1993).
[29] J. T. Karpen, R. B. Dahlburg, and J. M. Davila, Astrophys. J. **421**, 372 (1994).
[30] P. G. Drazin, J. Fluid Mech. **8**, 130 (1960).
[31] W. Horton, T. Tajima, and T. Kamimura, Phys. Fluids **30**, 3485 (1987).
[32] X. L. Chen and P. J. Morrison, Phys. Fluids B **2**, 495 (1990).
[33] X. L. Chen and P. J. Morrison, Phys. Fluids B **2**, 2575 (1990).
[34] A. P. Singh and S. P. Talwar, Sol. Phys. **149**, 331 (1994).
[35] A. P. Singh and S. P. Talwar, Phys. Plasmas **3**, 447 (1996).
[36] R. B. Dahlburg, S. K. Antiochos, and T. A. Zang, Astrophys. J. **383**, 420 (1991).
[37] R. B. Dahlburg, S. K. Antiochos, and T. A. Zang, Phys. Fluids B **4**, 3902 (1992).
[38] S. A. Orszag, J. Fluid Mech. **50**, 689 (1971).
[39] R. B. Dahlburg, T. A. Zang, D. Montgomery, and M. Y. Hussaini, Proc. Natl. Acad. Sci. U.S.A. **80**, 5798 (1983).
[40] R. B. Dahlburg, T. A. Zang, and D. Montgomery, J. Fluid Mech. **169**, 71 (1986).
[41] C. Lanczos, *Applied Analysis* (Prentice-Hall, New York, 1956).
[42] J. Gary and R. Helgason, J. Comput. Phys. **5**, 169 (1970).
[43] P. G. Drazin and W. H. Reid, *Hydrodynamic Stability* (Cambridge University Press, Cambridge, 1981).
[44] H. B. Squire, Proc. R. Soc. London, Ser. A **142**, 621 (1933).
[45] R. B. Dahlburg and J. T. Karpen, J. Geophys. Res. **100**, 23489, DOI: 10.1029/95JA02496 (1985).
[46] N. Seehafer and J. Schumacher, Phys. Plasmas **5**, 2363 (1998).
[47] D. W. Hughes and S. M. Tobias, Proc. R. Soc. London, Ser. A **457**, 1365 (2001).
[48] J. C. Perez, W. Horton, R. Bengtson, and T. Carter, Phys. Plasmas **13**, 055701 (2006).
[49] D. Montgomery, Phys. Scr. **T2/2**, 506 (1982).